J Solid State Electrochem (2009) 13:1267–1272
DOI 10.1007/s10008-008-0661-9

ORIGINAL PAPER

Detecting unalloyed tin in $LiSn_2(PO_4)_3$-based anodes with Mössbauer spectroscopy

Christopher M. Burba · Roger Frech · Agneta Seidel · Lennart Häggström · Anton Nytén · John O. Thomas

Received: 18 April 2008 / Revised: 15 August 2008 / Accepted: 24 August 2008 / Published online: 17 September 2008

Abstract The first discharge of the Li^+ ion anode material $LiSn_2(PO_4)_3$ was investigated with Mössbauer spectroscopy and electrochemical techniques. Mössbauer spectroscopy provided insight into the structure of the tin atoms of the fully discharged anode materials. Spectra consist of overlapping peaks, which are assigned to noncrystalline β-Sn and Li–Sn alloy domains. An analysis of the relative intensities of the Mössbauer spectra shows the relative abundance of β-Sn increases at the expense of the Li–Sn alloy as the discharge rate increases. Cell polarization occurs at higher discharge rates, leading to inefficient electrode utilization and poor cycling performance. Sluggish Li^+ ion diffusion through the amorphous Li_3PO_4 network that is formed early in the discharge process might be responsible for the poor electrochemical performance and the accumulation of unalloyed tin.

Keywords Lithium ion batteries · Anodes · $LiSn_2(PO_4)_3$ · Mössbauer spectroscopy

C. M. Burba (✉)
Department of Natural Sciences, Northeastern State University,
600 N. Grand Ave.,
Tahlequah, OK, 74464, USA
e-mail: burba@nsuok.edu

R. Frech
Department of Chemistry and Biochemistry,
University of Oklahoma,
620 Parrington Oval, Room 208,
Norman, OK, 73071, USA

A. Seidel · L. Häggström
Department of Physics, Uppsala University,
P.O. Box 530, 751 21, Uppsala, Sweden

A. Nytén · J. O. Thomas
Department of Materials Chemistry, Uppsala University,
P.O. Box 538, 751 21, Uppsala, Sweden

Present address:
A. Seidel
Swedish Patent and Registration Office,
P.O. Box 5055, 102 42, Stockholm, Sweden

Introduction

There are significant efforts to identify high-capacity anode materials for lithium rechargeable batteries that are both safe and cost effective. Of course, lithium metal anodes offer the highest capacity and would be an excellent option if capacity were the determining factor in selecting an anode material. However, numerous studies have documented the serious safety concerns of lithium ion batteries that incorporate lithium metal anodes. Carbonaceous anodes are generally viewed as much safer than lithium metal and offer reasonable capacities. The theoretical discharge capacity of a carbonaceous anode is limited to 372 mAh/g, corresponding to a discharge product of LiC_6. The degree of crystallinity of the carbon material and the processing conditions used to prepare the material both strongly affect the capacity and cyclability of the anode materials, leading to some variability in the practical capacities achieved with carbonaceous materials. Alternative materials that offer higher capacities than the carbon-based technologies and pass the stringent safety requirements for commercialization are being aggressively pursued.

Lithium-metal alloys have been suggested as a potential means of achieving high capacities while maintaining safety standards. In addition to high capacities, lithium-metal alloys often offer sufficiently low lithium reduction potentials to be competitive with graphitic anode materials. For example, lithium and tin alloy to a maximum

composition of $Li_{22}Sn_5$ [1, 2], and can deliver a theoretical capacity of 993 mAh/g. Unfortunately, metallic tin anodes undergo excessive volume fluctuations (~400%) during the discharge process, which can result in significant particle cracking and disintegration [3, 4]. Over several cycles, the effects of the volume fluctuations accumulate and reduce the practical capacity of the anodes. One approach to circumvent this problem is to form a composite tin-based anode [5]. In this method, the composite tin-based compound first reacts irreversibly with lithium to form domains of metallic tin embedded within an inorganic matrix. The nano-domains of tin are then available to alloy with lithium to form a maximum composition of $Li_{22}Sn_5$ [6]. The inorganic matrix helps to preserve the structural integrity of the electrode particles during the extreme volume fluctuations in tin domains that are associated with cycling the battery [3]. Although this method is successful in reducing particle fragmentation, some of the anode's reversible capacity must be sacrificed to form the inorganic domains.

Since there are virtually no limitations on the constituents of a composite, tin-based anode, a very large number of materials have been examined. Recent thermal experiments on one candidate, $LiSn_2(PO_4)_3$, revealed residual metallic tin in fully discharged electrodes [7]. Mössbauer spectroscopy is an excellent analytical tool for probing the local structure of tin atoms in these types of compounds, since tin atoms surrounded by lithium atoms exhibit different isomer shifts than metallic tin (β-Sn). In this study, ^{119}Sn Mössbauer spectroscopy is combined with electrochemical techniques to further understand the local environment of the tin atoms present in discharged $LiSn_2(PO_4)_3$ electrodes as a function of discharge rate. This investigation will provide important insights into the nature of the tin atoms in discharged composite tin-based anodes.

Experimental methods

Samples of $LiSn_2(PO_4)_3$ were synthesized by a solid-state reaction of SnO_2, Li_2CO_3, and $(NH_4)_2HPO_4$. Stoichiometric quantities of the precursors were heated under static air at 400 °C for 3 h and then raised to 1250 °C (10 °C/min). The materials were annealed at 1250 °C for 48 h under static air. The synthesis procedure produced a mixture of the $P\bar{1}$ and $R\bar{3}c$ phases of $LiSn_2(PO_4)_3$. The $R\bar{3}c$ phase was converted to the thermodynamically stable $P\bar{1}$ phase by applying pressure (~1.4×10^8 Pa) with a KBr pellet press [8]. Phase purity was confirmed with powder X-ray diffraction (Scintag X'Tra X-ray diffractometer).

Electrochemical tests were performed with an Arbin battery cycler. Electrodes were prepared by mixing 87 wt.% $LiSn_2(PO_4)_3$, 5 wt.% KS-6 graphitic carbon (TimCal, Ltd.), 5 wt.% Super P, and 3 wt.% Teflon. The resulting mixture was then pressed into a thin sheet. Circular disks (1.27 cm^2) were cut from the sheet and dried overnight in a vacuum oven. Size 2430 coin cells were constructed using lithium foil as the anode and 1.0 M $LiPF_6$ in a 1:1 mixture of ethylene carbonate and dimethyl carbonate as the electrolyte. Samples were galvanostatically discharged at 0.05, 0.25, and 0.50 mA/cm^2 until the cell potential was less than 0.01 V vs. Li^+/Li. Afterwards, the coin cells were disassembled and stored under an inert atmosphere.

^{119}Sn Mössbauer measurements with a $Ca^{119}SnO_3$ source (10 μCi) were performed at room temperature in transmission geometry and constant acceleration mode. Care was taken to protect the samples from the atmosphere during transit to the Mössbauer spectrometer. Velocity calibration was performed using a ^{57}Co*Rh* source and the resonance lines of α-Fe as velocity standards. All spectra were analyzed with routine least-square fitting programs, and all reported Sn isomer shift values refer to a $BaSnO_3$ standard at room temperature.

Results and discussion

Electrochemical data

The first discharge of $LiSn_2(PO_4)_3$ is presented in Fig. 1. Behm and Irvine [9] have previously reported the electrochemical performance of $LiSn_2(PO_4)_3$, and our results agree well with their findings. Upon discharging at 0.05 mAh/g, the $LiSn_2(PO_4)_3$ cells undergo a voltage plateau at approximately 1.49 V vs. Li^+/Li (region I of Fig. 1), corresponding to reduction of Sn^{4+} ions to metallic tin nano-domains embedded within a disorganized Li_3PO_4 matrix [9]. Accordingly, the discharge capacity of the cells at the end of the first plateau is equivalent to four lithium atoms for each tin atom in the anode. A small, secondary

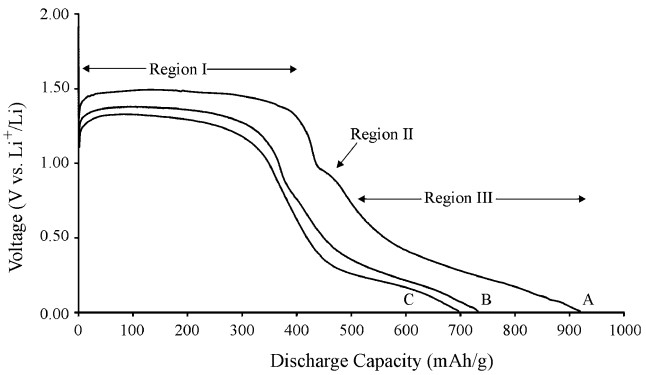

Fig. 1 Discharge curves for $LiSn_2(PO_4)_3$ recorded at **a** 0.05, **b** 0.25, and **c** 0.50 mA/cm^2

plateau is observed near 0.95 V and denoted as region II on the figure. This region is attributed to electrolyte decomposition reactions that take place on the surface of the electrode particles to form a solid electrolyte interphase (SEI) layer [7]. Below ~0.90 V, lithium atoms form Li–Sn alloys with the tin domains according to the Li–Sn phase diagram, and the cell voltages gradually decrease to 0.01 V (region III) [6, 10]. A total first discharge capacity of 919 mAh/g is measured for cells discharged at 0.05 mA/cm^2. Differential capacity plots often illuminate details that are difficult to discriminate from the voltage vs. capacity curves; therefore, the first derivative of each discharge curve is constructed and presented in Fig. 2. In these plots, region I appears as an intense negative peak early in the discharge process, whereas capacity due to deposition of the SEI layer on the $LiSn_2(PO_4)_3$ particles is attributed to a small peak between 1.00 and 0.80 V. The formation of Li–Sn alloys is associated with broad, overlapping peaks at low potentials in Fig. 2.

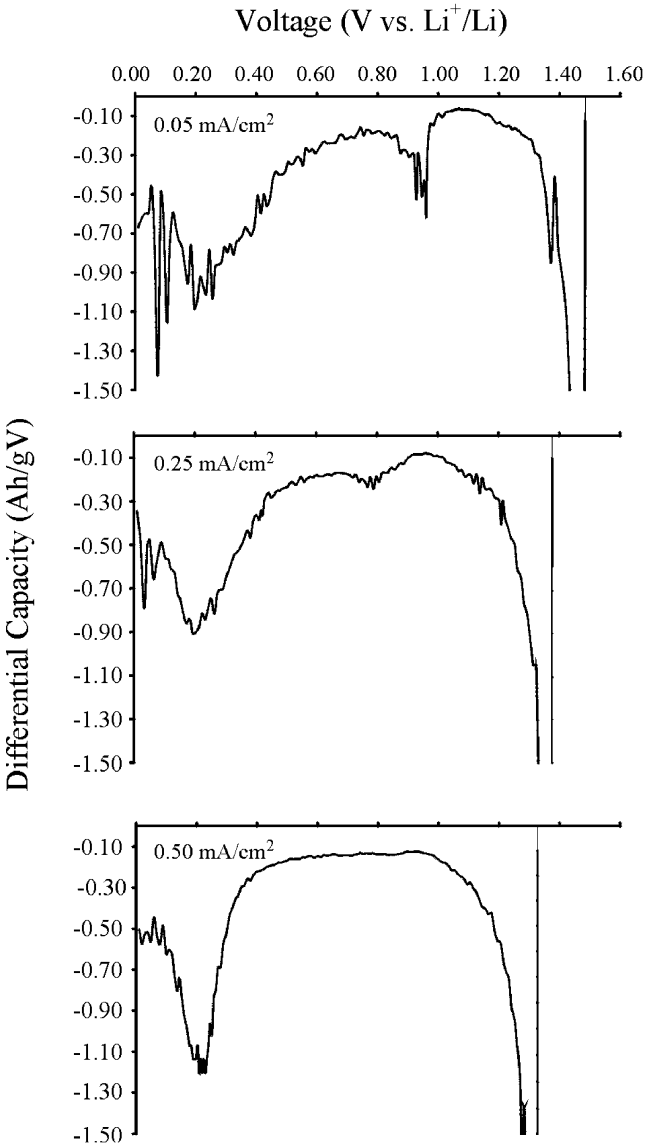

Fig. 2 Differential capacity plots of $LiSn_2(PO_4)_3$ discharged at 0.05, 0.25, and 0.50 mA/cm^2

Increasing the discharge rate affects both the overall cell discharge capacities as well as the cell potentials. For example, voltage plateaus recorded during region I decrease from 1.49 V (0.05 mA/g) to 1.37 and 1.32 V when cells are discharged at 0.25 and 0.50 mA/cm^2, respectively. In addition, faster rates result in smaller overall discharge capacities. Relative fractions of the total capacity for each rate are calculated with the aid of the differential capacity curves (Fig. 2) and are presented in Table 1. For example, voltage cutoffs for each region of the 0.25 mA/cm^2 curve are selected from Fig. 2 as follows: open circuit voltage to 1.00 V (region I), 1.00 to 0.60 V (region II), and 0.60 to 0.01 V (region III). Theoretical predictions of the discharge capacity for regions I and III are also included in Table 1 for comparison. These calculations assume: (1) $LiSn_2(PO_4)_3$ and Li first react to produce only Li_3PO_4 and metallic tin and (2) all of the tin nano-domains alloy with lithium up to a maximum composition of $Li_{22}Sn_5$. The theoretical discharge capacities of regions I and III for $LiSn_2(PO_4)_3$ are 405 and 446 mAh/g, respectively. The theoretical values presented in Table 1 are merely to be used as a reference point for comparing the discharge capacities of the three regions from Fig. 1 since it is possible that alloys with a smaller Li/Sn ratio will be formed during the discharge process. Capacities in excess of the theoretical predictions are detected in region I for cells discharged at the slowest rate. The additional capacity might be related to decomposition reactions occurring at higher potentials (e.g., see Fig. 2 between 1.20 and 1.40 V) [11]. However, the exact reason for the additional capacity is unknown at this time. The fraction of capacity attributed to region I falls below the theoretical predictions with increasing discharge rate.

The relative proportion of capacity due to the electrolyte decomposition reactions (region II) also depends on the discharge rate. Beattie et al. [11] speculated that electrolyte decomposition is catalyzed by metallic tin moieties within

Table 1 Discharge capacities (mAh/g) of $LiSn_2(PO_4)_3$ anodes. Regions I, II, and III correspond to Fig. 1

	0.05 mA/cm^2	0.25 mA/cm^2	0.50 mA/cm^2	Theoretical
Region I	429	370	362	405
Region II	78	59	42	0
Region III	412	304	293	446
Total capacity	919	732	697	851

the partially discharged electrodes, and the decomposition reactions essentially cease after Li–Sn alloys form. Consequently, electrolyte decomposition is largely restricted to cell potentials that are low enough to form the metallic tin yet sufficiently high to prevent the formation of Li–Sn alloys (approximately 1.00 to 0.80 V). This hypothesis is supported by the appearance of CO_3^{2-} bands in the infrared spectrum of discharged $LiSn_2(PO_4)_3$ electrodes during region II [7]. These bands are attributed to decomposition products from the ethylene carbonate and dimethyl carbonate solvent molecules. Cells that are slowly discharged spend relatively longer periods of time within the voltage window wherein most of the decomposition occurs. Thus, these cells have larger region II capacities.

All of the $LiSn_2(PO_4)_3$ cells had region III capacities lower than the theoretical prediction for the formation of $Li_{22}Sn_5$. At the lowest discharge rate, the cells delivered 92% of this theoretical capacity. If the cells did indeed form only $Li_{22}Sn_5$ domains, then approximately 8% of the tin domains are not alloyed at this discharge rate. The poor electrode utilization is exacerbated when cells are discharged at higher rates. For example, only 68% of the theoretical discharge capacity is achieved at 0.25 mA/cm^2 and 66% of the theoretical discharge capacity for cells discharged at 0.50 mA/cm^2. Although insight into the specific Li–Sn alloy formed during discharge cannot be elucidated from the electrochemical data, the combination of lower discharge potentials and poorer electrode usage at higher discharge rates (0.25 and 0.50 mA/cm^2) do point to significant polarization within the $LiSn_2(PO_4)_3$ cells. The polarization effects likely result from slow lithium diffusion through the amorphous Li_3PO_4 matrix that houses the tin nano-domains and/or the buildup of a resistive layer on the surface of the electrode particles, which presumably formed during region II.

Cycling performance of the $LiSn_2(PO_4)_3$ anodes is depicted in Fig. 3. Each compound had a high initial discharge capacity, but exhibited much lower discharge capacities on subsequent cycles. The discharge capacity of a cell cycling at 0.50 mA/cm^2 only delivered 103 mAh/g after the 20th cycle, and cells cycling at higher rates had somewhat lower discharge capacities. The cycling performance of these electrodes matches the results of Behm and Irvine for $LiSn_2(PO_4)_3$ [9].

Mössbauer spectroscopy

Transmission ^{119}Sn Mössbauer spectra of $LiSn_2(PO_4)_3$ electrodes recorded at room temperature (300 K) are presented in Fig. 4 to assess the local environment of the tin atoms. At a very low discharge rate (0.05 mA/cm^2), the Mössbauer spectrum is dominated by an intense peak centered at about 1.9 mm/s with a weak shoulder at about

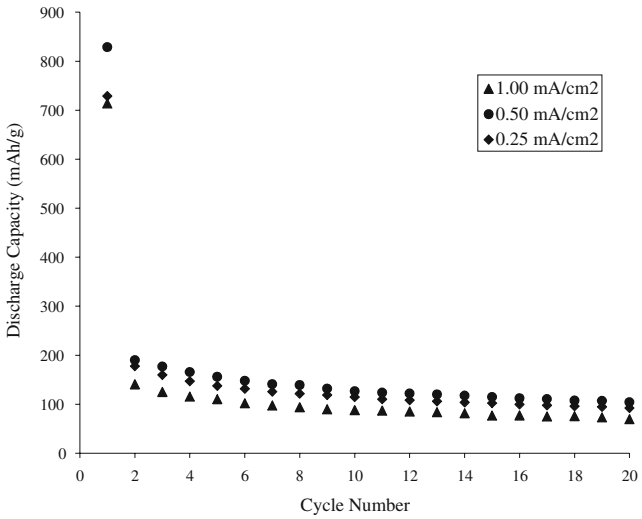

Fig. 3 Discharge capacities of $LiSn_2(PO_4)_3$ anodes as a function of cycle number. The anodes were cycled at room temperature

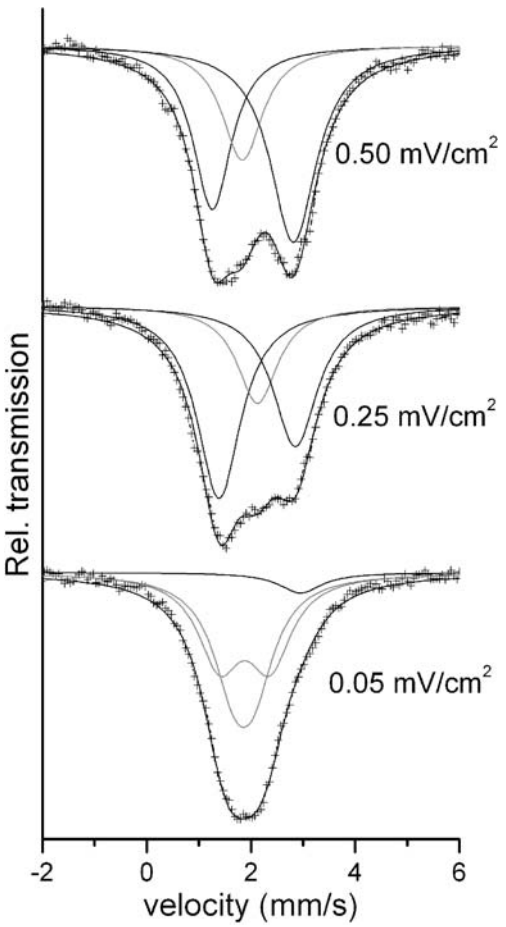

Fig. 4 ^{119}Sn Mössbauer spectra of fully discharged $LiSn_2(PO_4)_3$ electrodes. Discharge rates are given in the figure. Assignments of the resonance lines are provided in the text

2.8 mm/s. There is no evidence of Sn^{4+} ions in the Mössbauer spectra of the fully discharged electrodes based on the lack of spectral intensity near 0 mm/s. Thus, the Sn^{4+} cations in the as-prepared $LiSn_2(PO_4)_3$ electrodes are completely reduced during the first discharge, and the electrodes were not oxidized during data collection.

In a recent paper, several Li–Sn crystalline phases have been carefully studied by Mössbauer spectroscopy [12]. The present spectrum most closely resembles the spectrum of Li_7Sn_2 in [12], which also shows a marked high velocity shoulder. Our spectrum was, therefore, analyzed as originating in Li_7Sn_2 with two tin sites of equal occupancy. A single line at the high velocity side of the spectrum was introduced to provide a good fit with the spectrum. This single line has an isomer shift of 2.85 mm/s, which is a bit larger than crystalline β-Sn (2.56 mm/s). It is well known that the isomer shift for noncrystalline β-Sn differs from crystalline β-Sn. Therefore, the immediate interpretation is that the final discharge product of $LiSn_2(PO_4)_3$ at low rates consists of Li_7Sn_2 and noncrystalline β-Sn. The Li–Sn compound typically anticipated in fully discharged composite tin anodes is $Li_{22}Sn_5$. This compound may be ruled out as a possible product since the isomer shift and quadrupole splitting reported for $Li_{22}Sn_5$ is 1.83 and 0 mm/s, [12], and we observe an average isomer shift and average quadrupole splitting of 1.88(2) mm/s and 0.67 (5) mm/s, respectively. A similar observation of Li_7Sn_2 as an end compound has been reported in the discharge of η-Cu_6Sn_5 anodes [12]. The observed spectral intensities of the Mössbauer spectra for the slowest discharge rate are found to be I(β-Sn)=6(2)% and I(Li_7Sn_2)=94(2)%. The individual Lorentzian line full widths at half maximum (FWHM) were 0.95 (2) mm/s.

When the discharge rate is increased to 0.25 and 0.50 mA/cm^2, the spectral peaks broaden towards lower velocity and the shoulder on the high velocity side develops into a resolved peak. The two spectra were fit with three single lines with Lorentzian line widths (FWHM) of approximately 0.95(2) mm/s. We interpret the two low-velocity lines of each spectrum as Sn atoms in slightly different Li–Sn alloy domains and the high velocity line at 2.84(5) mm/s as noncrystalline β-Sn. The values for the isomer shift of the lowest velocity lines are 1.39(5) mm/s and 1.26(5) mm/s for the samples having discharge rates 0.25 and 0.50 mA/cm^2, respectively. Such low values for the isomer shift are not found in any of the Li–Sn crystalline phases studied to date; the lowest reported value is 1.83 mm/s for $Li_{22}Sn_5$ [12]. The Sn isomer shift decreases almost linearly for increasing Li content; therefore, our observed isomer shift values may come from Sn atoms in extremely lithium-rich, noncrystalline surroundings. The isomer shift values for the 2.13(5) and 1.84 (5) mm/s lines of the 0.25 and 0.50 mA/cm^2 samples fall within the range of crystalline Li–Sn alloys. These spectral features may therefore emanate from Sn atoms in more crystalline-like Li–Sn compounds. Observed spectral intensities for the three discharge rates are provided in Table 2.

Relative atomic fractions of the noncrystalline β-Sn and the Li–Sn domains can be calculated from the relative spectral intensities if each compound's Lamb–Mössbauer factor (i.e., recoil free fraction *f*) is known. At room temperature, the f-factor for β-Sn is extremely low: *f*(β-Sn)=0.04(1) [13]. The reported *f* factors for the Li–Sn compounds are scarce but exist for the compound $Li_{22}Sn_5$. Hightower et al. reported a room temperature *f*-factor ratio of *f*(β-Sn)/*f*($Li_{22}Sn_5$)=0.5(1) [14]. Assuming this ratio holds for noncrystalline β-Sn and the Li–Sn compounds formed in these samples, the atomic fractions may be calculated for discharged $LiSn_2(PO_4)_3$ anodes. The results of the analysis are presented in Table 2. The lowest discharge rate yielded electrodes with a high fraction of Li_7Sn_2 domains (89%), while higher discharge rates gives lower abundances of Li–Sn domains. For example, electrodes discharged at 0.50 mA/cm^2 consist of only 38% Li–Sn alloy.

The relative abundances provided in Table 2 are qualitative estimates of the amount of noncrystalline β-Sn and Li–Sn domains present in the fully discharged $LiSn_2(PO_4)_3$ electrodes. Limitations of using this approach to quantify the relative abundance of each domain within a composite tin-based anode have been discussed by Hightower et al. [14]. In addition, the crystallographic symmetry about a tin atom strongly influences its Mössbauer spectrum; thus, different spectra are expected for the various Li_xSn phases [12]. It is also possible the Li–Sn domains present in discharged $LiSn_2(PO_4)_3$ electrodes have

Table 2 Relative intensities and abundances of the metallic Sn and Li–Sn domains in fully discharged $LiSn_2(PO_4)_3$ electrodes as determined by Mössbauer spectroscopy

Rate (mA/cm^2)	Relative spectral intensity			Relative abundance		
	β-Sn	Crystalline Li–Sn alloy	Noncrystalline Li–Sn alloy	β-Sn	Crystalline Li–Sn alloy	Noncrystalline Li–Sn alloy
0.05	6(2)	94(2)	0	11(5)	89(5)	0
0.25	34(4)	22(4)	44(4)	51(9)	16(9)	33(9)
0.50	46(4)	23(4)	31(4)	62(8)	16(9)	22(9)

different recoil-free fractions. Regardless of this situation, the Mössbauer data clearly show a significant amount of unalloyed tin in the samples, particularly for cells discharged at relatively high rates (0.25 and 0.50 mA/cm^2), and this observation is in good agreement with the low discharge capacities observed for $LiSn_2(PO_4)_3$ electrodes discharged at these rates and the thermal measurements reported by Burba and Frech for this compound [7].

Conclusions

Electrochemical measurements recorded during the first discharge of $LiSn_2(PO_4)_3$ electrodes reveal significant cell polarization and inefficient electrode utilization when cells are discharged at 0.25 and 0.50 mA/cm^2. Cell polarization and poor cycling performance is attributed to sluggish Li^+ ion diffusion through the amorphous Li_3PO_4 network. It is also possible that electrolyte decomposition products, which form between 1.00 and 0.70 V, accumulate on the surface of the electrode forming a resistive SEI layer that inhibits Li^+ diffusion into the electrode particles. Although the cycling performance of $LiSn_2(PO_4)_3$ anodes does not rival carbon-based anodes, the Mössbauer spectra provide important insights into the local structure surrounding the tin atoms in a fully discharged composite anode.

Further insight into the reactions associated with the discharge process was achieved with Mössbauer spectroscopy, wherein it was possible to discriminate between the alloyed and unalloyed tin domains in the discharged electrodes. The lack of Sn^{4+} ions in all of the Mössbauer spectra—even at high discharge rates—suggests that the Sn^{4+} cations of $LiSn_2(PO_4)_3$ are efficiently reduced during the discharge process. Mössbauer spectra of $LiSn_2(PO_4)_3$ discharged to 0.01 V at 0.05 mA/cm^2 indicate that noncrystalline β-Sn and Li_7Sn_2 are the primary discharge products. Faster discharge rates increase the relative amount of noncrystalline β-Sn in the discharged samples. Furthermore, two different Li–Sn alloy domains are detected, one of which might be due to tin atoms surrounded by an extremely lithium-rich environment.

References

1. Gasior W, Moser Z, Zakulski W (1996) J Non-Cryst Solids 205–207:379 doi:10.1016/S0022-3093(96)00446-2
2. Sangster J, Bale CW (1998) J Phase Equil 19:70 doi:10.1361/105497198770342788
3. Beaulieu LY, Beattie SD, Hatchard TD, Dahn JR (2003) J Electrochem Soc 150:A419 doi:10.1149/1.1556595
4. Wolfenstine J, Foster D, Read J, Behl WK, Luecke W (2000) J Power Sources 87:1 doi:10.1016/S0378-7753(99)00359-6
5. Idota Y, Kubota T, Matsufuji A, Maekawa Y, Miyasaka T (1997) Science 276:1395 doi:10.1126/science.276.5317.1395
6. Courtney IA, Dahn JR (1997) J Electrochem Soc 144:2045 doi:10.1149/1.1837740
7. Burba CM, Frech R (2005) J Electrochem Soc 152:A1233 doi:10.1149/1.1914753
8. Morin E, Angenault J, Couturier JC, Quarton M, He H, Klinowski J (1997) Eur J Solid State Inorg Chem 34:947
9. Behm M, Irvine JTS (2002) Electrochim Acta 47:1727 doi:10.1016/S0013-4686(02)00017-8
10. Courtney IA, Tse JS, Mao O, Hafner J, Dahn JR (1998) Phys Rev B 58:15583 doi:10.1103/PhysRevB.58.15583
11. Beattie SD, Hatchard T, Bonakdarpour A, Hewitt KC, Dahn JR (2003) J Electrochem Soc 150:A701 doi:10.1149/1.1569477
12. Robert F, Lippens PE, Olivier-Fourcade J, Jumas J-C, Gillot F, Morcrette M et al (2007) J Solid State Chem 180:339 doi:10.1016/j.jssc.2006.10.026
13. Hohenemser C (1965) Phys Rev 139:185 doi:10.1103/PhysRev.139.A185
14. Hightower A, Delcroix P, Caër GL, Huang C-K, Ratnakumar BV, Ahn CC et al (2000) J Electrochem Soc 147:2427